IMECE2013-67342

A NUMERICAL STUDY FOR BIOMIMETIC STRUCTURES TO CONTROL WALL SHEAR STRESS IN WATER

Matthew J. Gerber
Department of Mechanical and Aerospace Engineering
The Ohio State University
Columbus, Ohio, USA

ABSTRACT

There are numerous practical applications whose operational efficiency depends on the shear stress (skin friction drag) on their functional surfaces, including artificial reefs, artificial hearts, and continuous flow microbial fuel cells. For the most part, the fundamental physics that govern surface shear stress are well understood and established, especially for relatively simple shapes such as a sphere or cylinder. However, the use of passive, bio-inspired, additive structures to control surface shear stress has thus far seen limited investigation. To evaluate the effect of geometrical forms on surface shear stress, 29 biomimetic structures based on sharkskin, cacti, and ocean-dwelling suspension feeders were studied. The structures were modeled in COMSOL Multiphysics, and the shear stresses on their surfaces were studied. The results show that shear stress on the surface of a structure depends not only on surface area, but also on the general form of the structure. In addition, the surface shear stress of some structures display a strong dependence on fluid-flow orientation, while others do not.

INTRODUCTION

Wall shear stress (also known as skin friction drag) arises from the friction of a fluid against the surface of a solid object with either the fluid or the object in motion. The shear stress on a surface is directly related to the actual surface area of the liquid–solid interface in contact with the fluid, also known as the "wetted area." While the mechanics behind the connection of the wetted area to the surface shear stress are well understood [1, 2], the relationship of the geometrical form of the wetted area to the shear stress has received little investigation. A limited effort has been made [3] to draw connections between the geometry of structures and shear stress, but only in the context of specific biological systems and without a general, widely applicable engineering focus to an underlying dependence of passive, additive structures on shear stress. Nevertheless, there are numerous practical applications whose operational efficiency is dependent on the shear stress on their functional surfaces. In addition, there are many applications that require specific regimes of shear stress on their surfaces depending on flow direction. Examples include oceanic artificial reefs, human-implanted artificial hearts, and continuous flow microbial fuel cells. In each of these applications, low shear stress on the liquid–solid interface is required. For example, to preserve oceanic ecosystems, artificial reefs are being developed and embedded on the seabed. A typical seabed experiences large values of Reynolds numbers (1.5×10^4 to 3.0×10^5), a continuous flow microbial fuel cell experiences small values of Reynolds numbers (10–300), and the chambers of an artificial heart experience moderate values of Reynolds numbers (1000–5000). Therefore, a variety of flow conditions exist depending on the actual application.

An artificial reef is an underwater structure constructed to facilitate growth of marine ecological environments, control erosion, and proliferate available biological resources [4, 5]. The fluid flows experienced are turbulent with Reynolds numbers in the range of 1.5×10^4 to 3.0×10^5. To fulfill its intended purpose, it is necessary for an artificial reef to be an environment conducive to the growth of corals, algae, sponges, and other surface-growing organisms. A low shear stress on the surface of the artificial reef structures must be maintained to

assist new growth and prevent constructive bio-fouling from being sheared off.

An artificial heart is a device intended to either permanently replace a damaged natural heart or bridge the waiting time between heart removal and heart transplant. Unfortunately, artificial hearts are known to fail, and a major cause after implanting is clot formation [6]. It has been hypothesized that the connection between the chamber fluid flow and the *in vivo* clotting process of blood is partially the result of wall shear stress [6]. Studies over a range of Reynolds numbers typically experienced within such devices (1000–5000), show empirical and numerical relationships between wall shear stress or skin friction and formation of blood clots [7–9]. Results suggest that shear rates greater than 1×10^4 s^{-1} activate platelets and trigger clot formation [8].

A microbial fuel cell is a bio-electrochemical reactor that directly converts the chemical energy stored in organic compounds to electricity by means of microbial metabolism. Electron-producing bacteria grow in a biofilm adhered to the anode surface, and in the continuous flow configuration, a substrate-rich fluid is continuously flowed through the anodic chamber. A decrease in shear stress across the surface of the anode will allow for a higher growth rate of microorganisms, resulting in a net increase of power output density, which can be limited by the actual number density of microbes alive in the biofilm [10, 11]. In addition, the biofilm growth on the anode will decrease the efficiency of the fuel cell due to nutrient depletion and issues with bacterial waste removal, essentially clogging the flow through the fuel cell. For this reason, an anode structure with high surface shear stress in one fluid flow direction and low surface shear stress in the opposite fluid flow direction may be desirable. Specific operational regimes remain to be tested to show whether such an ability would allow bacteria growth under one flow direction, while providing a means to easily shear off the biofilm in the opposite, thereby extending the operational life of such devices.

To evaluate the effect of wetted area on shear stress, biomimetic structures were studied and the results are reported in this paper. For the most part, the fundamental physics behind surface shear rate and skin friction are well understood and established [1, 2]. However, the use of passive, additive structures to alter geometry to affect shear stress on a surface has thus far seen limited investigation. Furthermore, the mechanics of shear stress for three-dimensional structures such as a sphere or cylinder are also known [1, 12], but no comprehensive comparison of such additive structures (and other, more complicated geometries) for systematically controlling surface shear stress in a fluid flow exists in the literature. To study the effects of structural geometry on surface shear stress, it is first necessary to generate a diverse assortment of structures to study. One approach is to draw inspiration from nature as a source of geometrical structures. Biomimetic engineering is a field of study focused on learning from the design of nature to enhance the performance of engineering systems [13]. The belief is that nature's processes of evolution

and adaptation through natural selection have optimized specific biological systems for fulfilling vital necessities such as reproduction and survival. Here, passive structures that exhibit the ability to modify surface shear stress effects were investigated. Specifically, to engineer structures and geometries to systematically control surface shear stress, a variety of biological organisms were considered.
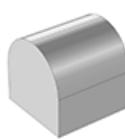
Based on the existing reports available for passive control methods (methods that require no external power input to operate) sharkskin was one biological mechanism that was investigated—specifically, the skin of fast-swimming sharks such as the blue shark (*Prionace glauca*) and the longfin mako shark (*Isurus paucus*) [14–18]. These skins are composed of individual, V-shaped scales called dermal denticles. The denticles are ribbed with longitudinal grooves oriented parallel to the flow direction and are spaced in regular intervals of 100–300 μm, approximately 200–500 μm in height [18]. Low surface shear stress is achieved by causing the velocity of the water near the scales to be lower in comparison to the water moving further away from the body due to low boundary slip. This difference in velocity causes formation of turbulent vortices or eddies, which are pinned at the points of the denticles, thereby reducing the shear stress on the surface of the sharkskin. Another example includes the saguaro cactus (*Carnegiea gigantea*), a large, tree-like cactus species native to the southwestern United States. Direct numerical simulations of cactus-shaped cylinders have shown that the deep ridges of certain cacti species have an effect on skin friction drag [19]. The cacti experience high wind velocities in desert windstorms and likely rely on their surface geometry to affect the surrounding flow. Due to the deficiency of water in their natural habitat, the root system of the cacti cannot be deep, and therefore the cacti must weather high-velocity fluid flows by affecting the flow rather than establishing structural support against it. Additionally, other systems include ocean-dwelling organisms of the phylum Cnidaria including gorgonians (sea whips or sea fans), sea anemones, corals, and other attached Cnidaria, which are passive "suspension feeders" that live off small organisms that pass nearby [20].

The purpose of this paper is to provide insight into the relationship of geometrical features to passively control surface shear stress.

DESCRIPTION OF THE PROBLEM AND METHODOLOGY

With a focus on revealing the underlying geometrical principles that are able to be manipulated to systematically control surface shear stress, a number of geometric shapes were added to a flat plate. Aside from these specific geometric shapes, additional configurations were considered by orientating the structures in distinct ways in the fluid flow. The total design space was 29 structures with orientations, as summarized in Table 1.

Copyright © 2013 by ASME

Table 1 The design space of all 29 structures to be studied, their sources of biological inspiration (if applicable), and their reference names used throughout this study. "O" denotes orientation. Fluid flow is from the bottom-left. A total of 29 cases were investigated.

Barn O1 Inspiration: Cactus	Barn O2 Inspiration: Cactus	Block	Cylinder	Dome Inspiration: Suspension feeders	Halfmoon O1 Inspiration: Suspension feeders
Cone Inspiration: Sharkskin	Crescent O1 Inspiration: Suspension feeders	Crescent O2 Inspiration: Suspension feeders	Halfmoon O2 Inspiration: Suspension feeders	Pyramid O1 Inspiration: Sharkskin	Pyramid O2 Inspiration: Sharkskin
Slice O1 Inspiration: Barnacles	Slice O2 Inspiration: Barnacles	Barnacle O1 Inspiration: Barnacles	Tombstone O1 Inspiration: Cactus	Tombstone O2 Inspiration: Cactus	Truncated Cylinder O1, Inspiration: Sharkskin
Barnacle O2 Inspiration: Barnacles	Tent O1 Inspiration: Barnacles	Tent O2 Inspiration: Barnacles	Truncated Cylinder O2, Inspiration: Sharkskin	Wedge O1 Inspiration: Sharkskin	Wedge O2 Inspiration: Sharkskin
Hexagon O1	Hexagon O2	Octagon	Pentagon O1	Pentagon O2	

To eliminate relative differences in physical size between structures, characteristic dimensions for each structure were normalized to 1 mm. Once the design space of structures was determined, a list of categories was generated to categorize the structures based on shape similarities to provide a basis for comparison. The geometrical differences studied were:

1. The general, structural form (cuboid, cylindrical, and triangular)
2. Facets (front, top, rear, and side) based on the general, structural form (cuboid, cylindrical, and triangular)
3. Two-dimensional shape of top facets (square, semicircle, crescent, and triangle)
4. Form of front and rear facet (flat, sloped, and cylindrical)
5. Total surface area

The structures were modeled in COMSOL Multiphysics 4.3 with the working fluid as water at standard conditions. The physical configuration and dimensions of the computational domain for modeling are shown in Figure 2.

The structures are exposed to an incoming, uniform, laminar flow with a Reynolds number of 300, representing a particular flow regime of interest for a target application in continuous flow microbial fuel cells, calculated with the hydraulic radius of open channel flow as the representative physical dimension. The governing equations for the fluid flow

are the continuity and incompressible, steady Navier–Stokes equations with body force neglected. The advection term is also neglected because, for the purpose of this study, particle transport properties are unimportant.

$$\nabla \cdot \bar{u} = 0$$
$$\nabla p = \mu \nabla^2 \bar{u} \qquad (1)$$

where $\bar{u}$ is the fluid velocity, ρ is the fluid density, p is pressure, and μ is the dynamic viscosity of the fluid [21]. The governing equations are essentially the continuity equation and Stokes' flow equations solved in the non-inertial frame of reference and at steady state.

It is important for any numerical simulation to ensure mesh insensitivity of the simulation results to increase model relevance and reduce error magnitudes and computation time. Consequently, an error evaluation was defined based on three relevant, representational values: average shear rate on the front face, minimum pressure on the rear face, and maximum velocity magnitude on the top face. Briefly, a coarse mesh was first created, then the model computed, and the three parameters values recorded. Then, the mesh was refined, the model solved again, and the values re-computed and recorded. The error was evaluated according to Equation 2:

$$\varepsilon = \frac{v_{new} - v_{prev}}{v_{prev}} \times 100\% \qquad (2)$$

where ε is the percent error, v_{new} is the value measured from the solution of the refined mesh, and v_{prev} is the value measured from the previous coarse mesh. The error threshold was set to 1%, and when mesh refinement produced an error of less than 1%, the mesh was considered adequately refined for the calculations. An example error analysis of the cone structure is shown in Figure 1.
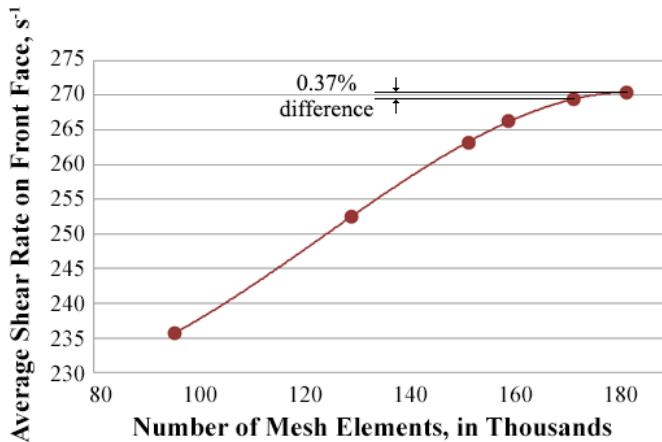

Figure 1: Numerical error analysis of the cone structure. The percent error between the 170,000-element mesh and 180,000-element mesh is less than 1%; therefore, the 170,000 element mesh was used for the study of this structure. The trendline is shown for clarity.

The shear stress to the surface due to the fluid is defined as

$$\tau_w = \mu \dot{\gamma} = \mu \left. \frac{\partial u}{\partial y} \right|_{y=0} \qquad (3)$$

where $\dot{\gamma}$ is the shear rate, u is the velocity of the fluid parallel to the surface, and y is the height above the surface [1].
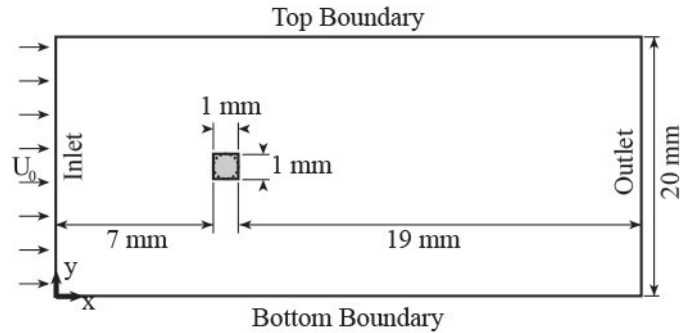
Figure 2: Schematic of the channel model for three-dimensional analysis of each structure with dimensions shown. The depth of the channel (out of the page) is 5 mm, with the structure located at the bottom of the channel under water.

RESULTS AND DISCUSSION

Figure 3 shows a representative contour plot for the average shear stress acting on the surface of the dome structure. The value of average shear stress used for most comparisons is the shear stress acting on a facet or facets of the structure averaged over the surface area of those surfaces.

Figure 4 shows the differences in total average shear stress between the general, structural forms (cuboid, cylindrical, and triangular), which correspond to item 1 in the design list summarized in Table 1. A single-factor ANOVA test was run on the results and a statistically significant difference exists between the mean shear stresses of the general structural forms ($p < 0.01$). The triangular forms exhibit the lowest average shear stress on their surfaces, owing to their lower surface areas (an average of 2.59 mm^2). However, the average surface area of the cuboid structures are nearly 20% larger than those of the cylindrical structures (4.53 mm^2 compared to 3.66 mm^2), yet the cylindrical structures exhibit larger (41%) average shear stress on their surfaces. The result implies that surface shear stress not only depends on the surface area but is also affected by the specific geometric shape.
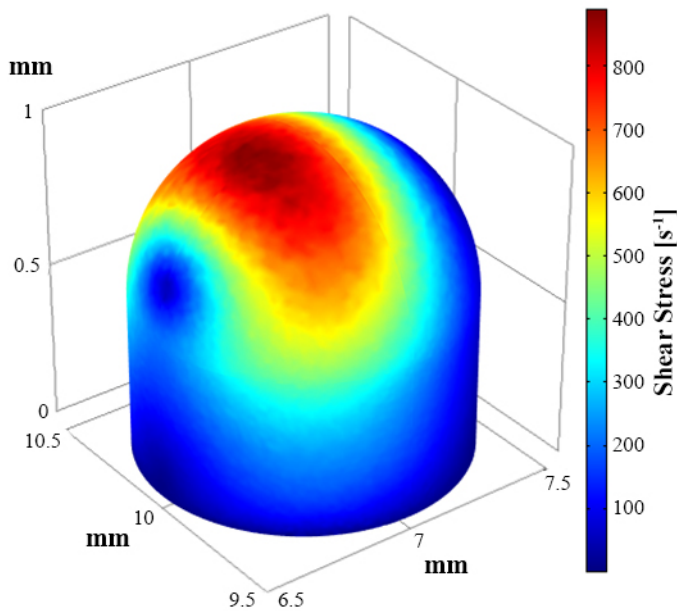
Figure 3: Aveage shear rate on the dome structure. Incoming fluid flow is from bottom-left.
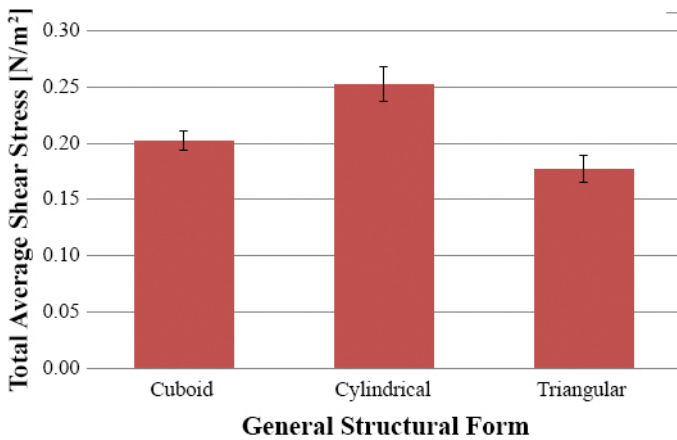
Figure 4: Total average shear stress on structures based on their general structural form: cuboid, cylindrical, and triangular. Error bars indicate one standard deviation to estimate uncertainty in the calculations.

Figure 5 summarizes the average shear stress on the structure facets (front, top, rear, and side) for each of the general forms (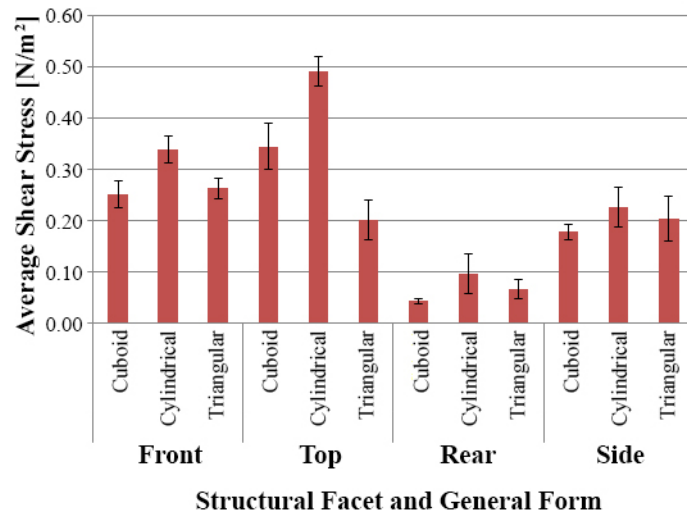cuboid, cylindrical, and triangular). These results correspond to item 2 in the design list. Here, "facet" refers to the effective surface plane relative to the flow: the front facet is normal to and is oriented towards the incident flow, the top facet is parallel to the incident flow, the rear facet is normal to and is oriented away from the incident flow, and the side facet is parallel to the incident flow and normal to the top and bottom. Only symmetrical structures were studied, and both side facets (left and right) were considered equivalent. For the front facet, the cuboid and triangular structures do not exhibit statistically different shear stress ($p < 0.01$), but the

cylindrical forms show a distinct shear stress. The implication for the observation of distinct shear stresses is that there is no difference between a cuboid or triangular form for low shear stress (< 0.3 N/m^2), but for high shear stress (> 0.3 N/m^2), a cylindrical form may be preferable as shown in the left panel in Figure 5. For the top facet, the cylindrical form exhibits greater shear stress than the cuboid and triangular forms (30% and 59% greater, respectively), but the triangular forms exhibit the lowest (less than half of the shear stress exhibited by the cylindrical structure), likely due to the fact that the triangular structures physically converge to a point or edge. Also, despite the cuboid forms having greater (51%) top-facet surface areas than the cylindrical forms, the cylindrical forms exhibit the greater average shear stresses, suggesting a dependence on the actual geometric form rather than the total surface area.

Figure 5 also shows a different trend for the rear facets. Here, the cylindrical forms may again exhibit the largest shear stresses, but the values have high variance (1.55×10^{-3} N/m^2), implying that in the wake region of a structure, vortices may play a more important role in determining the shear stress on a surface. Also, the cuboid structures exhibit the lowest shear stress on their rear facets (as opposed to triangular geometries for the top facet), which can be explained by the early separation point on the sharp edges of the rear facet as compared to a more rounded or cylindrical form. For the side facets, no statistically significant difference exists between any of the basic geometric features ($p \approx 0.13$), suggesting that the flow around these structures at the inlet Reynolds number does not affect the surface shear stress at the sidewalls.

Figure 5: Average shear stress of facets (front, top, rear, and side) based on the general, structural form (cuboid, cylindrical, and triangular). Error bars indicate one standard deviation to estimate uncertainty in the calculations.

To further elucidate the results in Figure 5, an additional two-dimensional calculation was performed to focus on the top surface for each structure with the representative data shown in Figure 6. This corresponds to item 3 in the design list above.

Copyright © 2013 by ASME

The semicircle, crescent, or triangle top facets yielded average stress values within 10% of each other. However, the square-top facet shape exhibits much smaller (35%) shear stress than the others. This result again demonstrates that shear stress is not an effect of surface area alone, as the average surface area of the square shapes are 68% larger than those of the semicircle, crescent, and triangle. The lower shear rate may also not be the result of edge effects, as the block and other square-top-facet structures have the same incident edge as slice O2 and other triangle-top-facet structures; nor can it be the result of separation point effects for similar reasons (geometric edge and point similarities between individual structures). Consequently, further investigation of flow around structures to investigate the role of vortices and pressure gradients due to the wake region is likely needed but is beyond the scope of this paper.
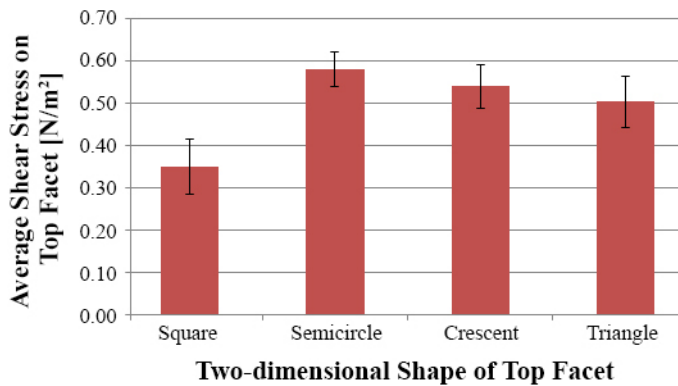
Figure 6: The average shear stress on the top facet as calculated from a two-dimensional calculation to further investigate effects described in Figure 5. All calculation conditions were matched to data presented in Figure 5. Error bars indicate one standard deviation to estimate uncertainty in the calculations.

The effect on shear stress on the front and rear facets is shown in Figure 7, with details on the specific forms summarized in Table 1. These results correspond to item 4 in the design list above. Here, "flat facet" refers to a facet that is vertically oriented and normal to the incident flow (e.g., the front facet of the block), "sloped" refers to a facet that is at an angle from the channel bottom (e.g., the front facet of Wedge O1), and "cylindrical" refers to a facet that is cylindrical in form (e.g., the front facet of the cylinder). For the front facets, there is little statistical difference between the flat and sloped facets ($p \approx 0.32$); however, the cylindrical face exhibits larger (63%) shear stress. In this case, the cylindrical front facet has a larger surface area than both the flat facets (by 60%) and the sloped facets (46%), suggesting a clear dependence of shear stress on surface area. Likewise, the surface stresses on the rear cylindrical facets are greater than the other two forms in addition to the surface areas on these facets. Furthermore, because the inlet flow geometry is normal to the front facet (Figure 2), the shear stress is highest at the front facet in comparison to the rear facet for all cases, as expected.
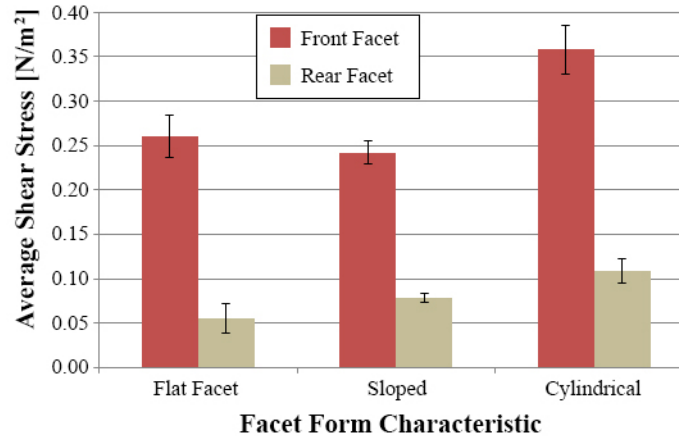
Figure 7: The average shear stress on the front and rear facets for the three general shapes of interest: flat facet, sloped, and cylindrical. Error bars indicate one standard deviation to estimate uncertainty in the calculations.
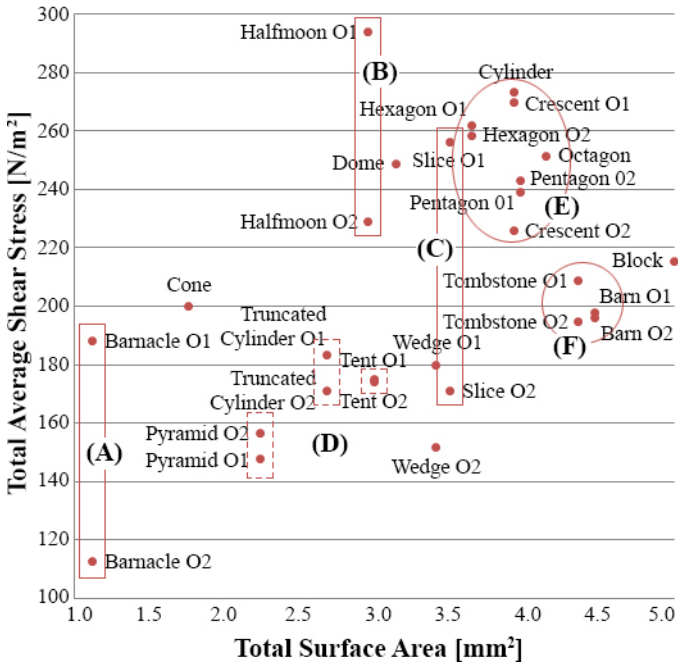
Finally, the total surface areas were plotted against the total average shear stress for all 29 cases evaluated in the design list. The results are shown in Figure 8.

Using the fourth-spread method [22] to quantitatively set the upper and lower boundaries to locate outliers in the dataset resulted in no apparent outliers. From an analysis based on linear regression, the coefficient of determination between the points was determined to be 0.223. This demonstrates that a linear relationship between the total surface shear stress and total surface area does not exist, as has been seen in previous results (Figures 3 and 4). The regression analysis implies that surface shear stress is not linearly dependent on surface area, and suggests that there may be another factor influencing the shear stress, namely the structural form.

From the solid boxes (A), (B), and (C), it can been seen that a few structures exhibit largely different shear stresses depending on their relative orientation to the fluid flow. For example, barnacle O1 has an average shear stress of 188.0 N/m^2 while barnacle O2 has an average shear stress of 112.7 N/m^2, a 40% difference. Likewise, the halfmoon structures have a 22% difference in their shear stress and the hlice structures have a 33% difference in their shear stress depending on the specific orientation as shown in Table 1. These results are in contrast to those of the three dotted boxes of (D), where a 6% difference exists for the pyramid structures, a 7% difference exists for the truncated cylinders, and a 0.6% difference exists for the Tent structures. Therefore, even though the structures are geometrically similar, there is a strong dependence on a structure's orientation in the fluid flow.

For the structures that exhibit the larger difference in shear stress (A, B, and C in Figure 8), the geometrical commonality is the form of the front and rear facets. For the orientation that results in higher shear stresses, all three structures have a vertically oriented edge that faces the incoming flow. As seen in Figure 9, this feature splits the incoming flow, separating it across the structure's front face. The rear face is flat and

vertically oriented in this orientation. The result is a fluid flow that affects the entire front facet of the structure. Likewise, for the orientation that results in a lower shear stress, all three structures have their flat, vertically oriented front face leading into the flow, and the edge is the rear face.

Figure 8: Total surface shear stress of a structure plotted against the total structure surface area for each of the 29 cases modeled.
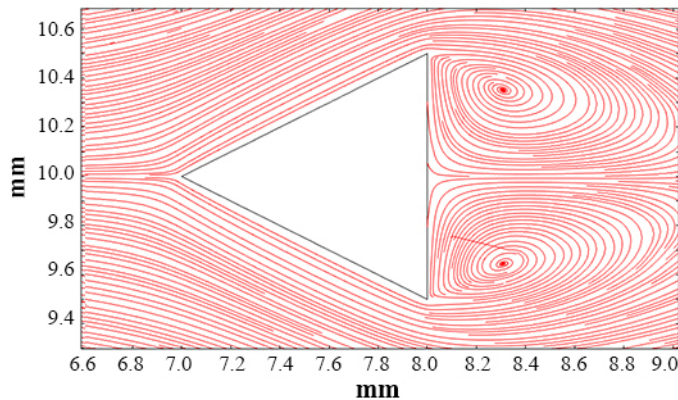
Figure 9: Flow separation around Slice O1 with incoming flow from the left. Cut plane depth is 0.5 mm from channel bottom.

In Figure 8, the circles (E) and (F) indicate groups of geometrically similar structural forms. (E) contains the cylindrical forms of the cylinder, hexagon O1, hexagon O2, pentagon O1, pentagon O2, octagon, crescent O1, and crescent O2. (F) contains the cuboid forms of tombstone O1, tombstone O2, barn O1, and barn O2. The shear stress depends strongly on the overall form more than it does on the differences in facet detail. For example, the barn shape is rectilinear while the tombstone shape is curvilinear, but their underlying geometric form is the same.

SUMMARY AND CONCLUSION

The results show that average surface shear stress (skin friction drag) on the surface of a structure depends not only on surface area, but also on the general form of the structure. For larger shear stresses, cylindrical forms are preferred, despite their smaller surface areas in comparison to other geometries. For lower shear stresses, there is little difference between cuboid and triangular shapes. For low shear stress on a top facet, a two-dimensional square shape results in the lowest shear stress. A cylindrical front facet and rear facet result in larger shear stresses on the surface of a structure due primarily to their surface areas. For some structures—such as the Barnacle, Halfmoon, and Slice—there is a strong dependence on their orientation in the fluid flow, while others—such as the Truncated Cylinder, Tent, and Pyramid—exhibit no such dependence. For applications that require a dependence on the fluid flow direction, a structure should have a leading edge on its front facet and a flat, vertically oriented rear facet for large surface shear stress. For decreasing the surface shear stress, the opposite is true.

REFERENCES

[1] White, F.M., 2003, *Fluid Mechanics*, Ed. 5, WCB/McGraw-Hill.

[2] Kundu, P.K., Cohen, I.M., and Dowling, D.R., 2011, *Fluid Mechanics*, Ed. 5, Academic Press.

[3] Vogel, S., 1994, *Life in Moving Fluids: The Physical Biology of Flow*, Princeton University Press.

[4] Zhao, T.Z., Mao, C.P., and Ping, J.X., 2011, "Study on Safe Weight of Artificial Reef in Different Water Depths and Bottom Slopes under Daya Bay Wave," Journal of Fisheries of China, **35**, pp. 1650–1657.

[5] Matsumoto, A., Mano, A., Mistui, J., and Hanzawa, M., 2012, "Stability Prediction on Armor Blocks for Submerged Breakwater by Computational Fluid Dynamics," Coastal Engineering Proceedings, **1** (33).

[6] Bachmann, C., Hugo, G., Rosenberg, G., Deutsch, S., Fontaine, A., and Tarbell, J. M., 2000, "Fluid Dynamics of a Pediatric Ventricular Assist Device," Artificial Organs, **24**, pp. 362–372.

[7] Orvim, U., Barstad, R.M., Orning, L., Petersen, L.B., Ezban, M., Hedner, U., and Sakariassen, K.S., 1997, "Antithrombotic Efficacy of Inactivated Active Site Recombinant Factor VIIa is Shear Dependent in Human Blood," Arteriosclerosis, Thrombosis, and Vascular Biology, **17**, pp. 3049–3056.

[8] Holme, P.A., Orvim, U., Hamers, M.J., Solum, N.O., Brosstad, F.R., Barstad, R.M., and Sakariassen, K.S., 1997, "Shear-Induced Platelet Activation and Platelet Microparticle Formation at Blood Flow Conditions as in Arteries with a Severe Stenosis," Arteriosclerosis, Thrombosis, and Vascular Biology, **17**, pp. 646–653.

[9] Badimon, L., Badimon, J.J., Galvez, A., Chesebro, J.H., and Fuster, V., 1986, "Influence of Arterial Damage and Wall Shear Rate on Platelet Deposition," Arteriosclerosis, **6**, pp. 312–320.

[10] Logan, B.E., 2009, "Exoelectrogenic Bacteria that Power Microbial Fuel Cells," Nature Reviews Microbiology, 7, pp. 375–381.

[11] Logan, B. E., Hamelers, B., Rozendal, R., Schröder, U., Keller, J., Freguia, S., Aelterman, P., Verstraete, W., and Rabaey, K., 2006, "Microbial Fuel Cells: Methodology and Technology," Environmental Science Technology, **40**, pp. 5181–5192.

[12] Munson, B.R., Rothmayer, A.P., Okiishi, T.H., Huebsch, W.W., 2012, *Fundamentals of Fluid Mechanics*, Ed. 7.

[13] Bar-Cohen, Y., 2006, "Introduction to Biomimetics: The Wealth of Inventions in Nature as an Inspiration for Human Innovation," Biomimetics: Biologically Inspired Technologies.

[14] Bhushan, B., 2009, "Biomimetics: Lessons from Nature—An Overview," Philosophical Transactions of the Royal Society, **367**, pp. 1445–1486.

[15] Lang, A.W., Motta, P., Hidalgo, P., and Westcott, M., 2008, "Bristled Shark Skin: A Microgeometry for Boundary Layer Control," Bioinspiration & Biomimetics, **3**, pp. 046005.

[16] Reif, W.E., 1982, "Morphogenesis and Function of the Squamation in Sharks, Comparative Functional Morphology of Shark Scales, and Ecology of Scales," Neues Jahrbuch für Geologie und Paläontologie, **164**, pp. 172–183.

[17] Reif, W.E., 1985, *Squamation and Ecology of Sharks*, Stuttgart: Senckenbergische Naturforschende Gesellschaft.

[18] Bixler, G.D. and Bhushan, B., 2013, "Fluid Drag Reduction with Shark-Skin Riblet Inspired Microstructured Surfaces," Advanced Functional Materials, **23** (19), pp. 1–22.

[19] P. Babu and K. Mahesh, 2008, "Aerodynamic Loads on Cactus-shaped Cylinders at Low Reynolds Numbers," Physics of Fluids, **20**, pp. 035112-9.

[20] Jørgensen, C.B. 1966 *Biology of Suspension Feeding* Pergamon Press, Oxford, UK, pp. 152–262.

[21] Wang, X.D., 2008, *Fundamentals of Fluid–Solid Interaction*, Elsevier BV.

[22] Devore, J.L., 2000, *Probability and Statistics for Engineering and the Sciences*, 5th ed. Duxbury, Pacific Grove, CA.